Opto-Electronic
Advances

CN 51-1781/TN ISSN 2096-4579 (Print) ISSN 2097-3993 (Online)

CW laser damage of ceramics induced by air filament

Chuan Guo, Kai Li, Zelin Liu, Yuyang Chen, Junyang Xu, Zhou Li, Wenda Cui, Changqing Song, Cong Wang, Xianshi Jia, Ji'an Duan and Kai Han

Citation: Guo C, Li K, Liu ZL, et al. CW laser damage of ceramics induced by air filament. *Opto-Electron Adv* **8**, 240296(2025).

https://doi.org/10.29026/oea.2025.240296

Received: 9 December 2024; Accepted: 21 April 2025; Published online: 27 June 2025

Related articles

Ultrafast dynamics of femtosecond laser-induced high spatial frequency periodic structures on silicon surfaces
Ruozhong Han, Yuchan Zhang, Qilin Jiang, Long Chen, Kaiqiang Cao, Shian Zhang, Donghai Feng, Zhenrong Sun, Tianqing Jia
Opto-Electronic Science 2024 **3**, 230013 doi: 10.29026/oes.2024.230013

Three-dimensional isotropic microfabrication in glass using spatiotemporal focusing of high-repetition-rate femtosecond laser pulses
Yuanxin Tan, Haotian Lv, Jian Xu, Aodong Zhang, Yunpeng Song, Jianping Yu, Wei Chen, Yuexin Wan, Zhaoxiang Liu, Zhaohui Liu, Jia Qi, Yangjian Cai, Ya Cheng
Opto-Electronic Advances 2023 **6**, 230066 doi: 10.29026/oea.2023.230066

More related article in Opto-Electronic Journals Group website

Opto-Electronic Advances

Article

July 2025, Vol. 8, No. 7

DOI: 10.29026/oea.2025.240296 CSTR: 32247.14.oea.2025.240296

CW laser damage of ceramics induced by air filament

Chuan Guo[1,2†], Kai Li[3†], Zelin Liu[1], Yuyang Chen[3], Junyang Xu[3], Zhou Li[3], Wenda Cui[1,2], Changqing Song[1,2], Cong Wang[3], Xianshi Jia[3*], Ji'an Duan[3] and Kai Han[1,2*]

Combined pulsed laser (CPL), introduced in 1975 for target damage, integrates different lasers to achieve high peak power and pulse energy. However, despite decades of research, CPL remains unused for long-range target damage due to the challenge of maintaining high peak power density over long distances. We note that a potential solution lies in leveraging the air filament generated by femtosecond laser, which can transmit peak power densities higher than 10^{14} W/cm^2 under the power clamping effect. To address this, a concept of a femtosecond laser induced air filament-CW CPL for surface damage of ceramics was introduced. We found no surface changes in ceramic targets when irradiated with a CW laser alone. By way of contrast, the target can be penetrated in a very short time (20 ms) with the assistance of the femtosecond laser induced air filament. In this context, we employ high-speed shadow imaging, cross-timescale simulation models and macro-microscopic characterization, to elucidate the CPL damage mechanism. The optimal CPL, combining a 1 mJ femtosecond laser and a 500 W CW laser, yields a damage rate of 1.51×10^7 μm^3/J, representing an improvement of approximately 175% compared to single femtosecond laser ablation and around 59% enhancement compared to coating-assisted CW laser ablation. Furthermore, the efficacy of the proposed femtosecond-CW CPL method is demonstrated in causing penetration damage of ceramic/metal composite material or direct damage of sapphire, showcasing its versatility in damaging applications. Consequently, the femtosecond-CW CPL ablation method presented in this paper holds great promise as a new type of damage method for transparent hard and brittle materials.

Keywords: laser damage; femtosecond laser; CW laser; combined pulse laser; ceramics

Guo C, Li K, Liu ZL et al. CW laser damage of ceramics induced by air filament. *Opto-Electron Adv* **8**, 240296 (2025).

Introduction

The study of laser-matter interaction is a long-standing, impactful field where each new discovery fosters diverse applications, underscoring the unique appeal of laser technology and processing research[1–3]. Laser-matter interactions are typically divided into two categories: long-pulse lasers characterized by high energy fluence (including continuous-wave (CW) laser), which excel in applications such as laser damage, welding, and additive manufacturing[4–6]; and short-pulse lasers characterized by high peak power density (including ultrafast laser), which are well-suited for micro-nano processing and subtractive manufacturing[7–10]. With advancements in techniques such as in-situ monitoring and spatial-temporal

[1]College of Advanced Interdisciplinary Studies, National University of Defense Technology, Changsha 400073, China; [2]Nanhu Laser Laboratory, National University of Defense Technology, Changsha 400073, China; [3]State Key Laboratory of Precision Manufacturing for Extreme Service Performance, College of Mechanical and Electrical Engineering, Central South University, Changsha 410083, China.

†These authors contributed equally to this work.

*Correspondence: XS Jia, E-mail: 221026@csu.edu.cn; K Han, E-mail: hankai0071@nudt.edu.cn

Received: 9 December 2024; Accepted: 21 April 2025; Published online: 27 June 2025

beam shaping, we are able to delve deeper into the underlying laser-matter interaction mechanisms while enhancing both processing efficiency and effectiveness[11–13]. These developments elevate the study of laser-matter interactions to new heights, revealing vast opportunities for practical application[14–16].

If high-energy lasers are compared to "1" and high-peak-power lasers to another "1," a natural question arises: how to achieve "1+1>2"? Combining high energy laser and high peak power laser to generate co-spatial and co-temporal outputs, referred to as combined pulsed lasers (CPL), may enable effects that cannot be achieved by the individual laser alone[17–19]. This concept is highly intriguing. However, it is not entirely novel. In 1975, Fox demonstrated the feasibility of this approach by combining a nanosecond laser with a CW laser, focusing both on the same metallic target. This combination induced transient penetration of metallic materials, reducing penetration time by two orders of magnitude compared to the CW laser alone[20]. Mechanisms such as enhanced absorption, recoil pressure and plasma shockwave were confirmed as fundamental to enhancing processing efficiency and effectiveness of the CPL[21–23]. For instance, in the study of laser-induced damage in BK7 glass, the material's low absorption of laser energy makes it challenging for a near-infrared millisecond laser alone to cause surface damage[24–26]. However, the introduction of surface defects via a high-peak-power nanosecond prepulse enables efficient damage by the millisecond laser[27]. Even more intriguingly, Ito et al. expanded this understanding through the electron dynamics modulation theory enabled by ultrafast laser. By forming filament inside transparent materials with a femtosecond laser, they generated high-density transient electrons that effectively deposited substantial energy from microsecond pulse[28]. This process achieved efficient surface damage or internal modification of transparent materials[29]. Since then, the exploration of CPL interactions with various materials has garnered significant attention, and applications have been successfully demonstrated in laser drilling, welding, grooving, and polishing[30–32].

In the context of the above considerations, we turn our attention to a specific application: high-energy laser damage. Two major challenges arise in this field: the first is improving damage efficiency (i.e., reducing laser power requirements), and the other is achieving efficient damage at long distances (i.e., increasing the laser power delivered to the target)[33]. As previously mentioned, the CPL method addresses the first challenge. However, this introduces a new issue: for the second challenge, ensuring that two laser beams can effectively transmit over long distances and deliver high power to the target is inherently more complex. It is noteworthy that, despite over fifty years of research, the CPL method has yet to be applied successfully for long-distance laser damage—an evident gap in the field. From the perspective of CPL transmission and interaction mechanisms, it is clear that assisted pulsed lasers with high peak power densities (>10^9 W/cm^2) can be easily generated in laboratory settings by focusing the lasers, yet they remain difficult to apply effectively for long-distance damage in practical scenarios[34,35]. The primary reason for this is beam dispersion, which leads to a loss of power density during long-distance transmission, rendering all current CPL methods ineffective for such applications. Therefore, new methods must be explored to overcome the practical challenges of long-distance transmission and efficient damage of the CPL damage method.

Let us revisit an important report from over two decades ago: as early as 2003, Kasparian et al. demonstrated filament transmission over distances of 20 km by focusing femtosecond laser in atmospheric[36]. The filament induced by a focused femtosecond laser has been shown to transmit over kilometer distances, forming kilometer-long filament in atmospheric environments[37]. The power density in the filament core stabilizes at approximately 10^{14} W/cm^2 due to the power clamping effect, which is sufficient to cause surface damage to most materials. However, for a single femtosecond beam, the clamping effect accompanying the filament limits the achievable damage efficiency[38]. The challenge lies in the fact that the damage efficiency is often constrained because most of the laser energy is absorbed by the excited plasma, preventing the energy from transferring further into the target material[39]. Thus, current high-energy femtosecond laser damage typically relies on electromagnetic pulses generated by the interaction between femtosecond laser and plasma, which induce strong currents on the metal casings of equipment, interfering with or damaging internal electronic components. However, when it comes to material hard damage, the efficiency remains very limited.

However, looking back at this report, a new idea might emerge: using high-energy femtosecond laser to ionize air and generate an air filament, which could then be combined with CW laser for long-range damage to the target. This approach might seem capable of addressing both challenges. However, several key questions remain unanswered: how will the power clamping effect of the filament influence the overall damage process? What impact will filament fragmentation at the tail end have? More importantly, could the plasma shield created by the filament counteract the CW laser, diminishing its effectiveness? Given these uncertainties, much further exploration is needed to determine whether the combination of femtosecond laser-induced air filament and CW laser can form a novel technological paradigm.

In this context, we present an innovative femtosecond-CW CPL method for surface damage, demonstrating high stability and efficiency in CW laser damage to ceramics, aided by the femtosecond laser-induced air filament. Structural or functional ceramics, including materials such as alumina ceramic, sapphire, exhibit characteristic traits of hardness, brittleness, and transparency[40]. They are extensively used in equipment and armor applications, such as alumina ceramic bodies and sapphire window mirrors. We compare the damage performance of femtosecond-CW CPL with single CW laser and femtosecond laser, through macro-microscopic characterization, quantitative analysis of damage rate, high-speed shadow imaging of dynamic processes, and multiphase hydrodynamic simulations. Additionally, we reveal, for the first time, the transient changes in CW absorption induced by surface defects prepared by femtosecond laser-induced air filaments, and analyze the time-scale variation of femtosecond-CW laser damage to the target. Finally, we demonstrate potential applications of the femtosecond-CW CPL damage method.

Materials and methods

Femtosecond-CW CPL setup

A schematic diagram of the femtosecond-CW CPL system is shown in Fig. 1. The setup involves the initial focusing of a 1080 nm CW laser (1000 W, fiber core 14 μm, NA 0.07, Sichuan DG Laser Technologies Co., LTD, China) and an 800 nm femtosecond laser (7 mJ, 1 kHz, 35 fs, M^2 1.4, Spectra-Physics, America), followed by their spatial combination using a dichroic mirror. The diameter of the focused CW laser is calculated to be 167 μm with a Rayleigh length of 1560 μm (focal length 500 mm). A DG645 (Stanford Research Systems, America) is used to control the synchronous output of the femtosecond laser and CW laser. A 5-degree-of-freedom motion stage was also used to moving the target for damage, with three

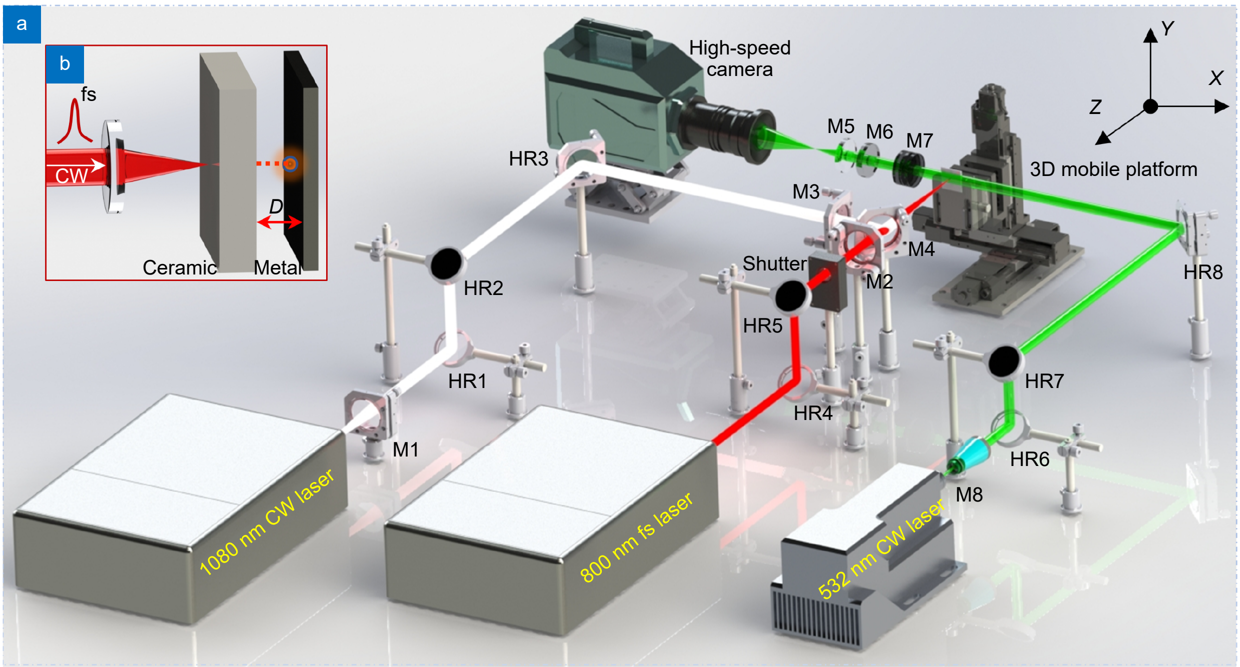

Fig. 1 | Schematic diagram of the femtosecond-CW CPL damage system. (**a**) M1 is a collimator for 1080 nm CW laser. HR1-8 are high reflectivity mirrors (R > 99.8%). M2 and M3 are the focusing mirrors (focal length 50/500 mm, diameter 25.4 mm). M4 is a dichroic mirror @ 1080 nm high reflectivity and 800 nm high transmittance. M5 is a lens (focal length 100 mm, diameter 25.4 mm) that matched the high-speed camera. M6 is a filter for passing 532 nm CW illumination laser. M7 are the attenuation mirrors. M8 is a 6× beam expander. (**b**) Schematic diagram of the femtosecond-CW CPL penetration damage experiment. A 304-SS metal plate is behind the ceramic target with distance of D (0, 5 mm).

translational degrees of freedom (Suruga Seiki Co., LTD, China). The spatial position of the CW laser beam waist is adjustable by moving the position of M3 (marked in Fig. 1(a)) to focus on the front, middle and tail positions of the filament, thus analyzing the corresponding damage rate (defined as the volume modified per unit pulse energy /1 J).

High-speed shadow imaging setup

A CW illumination laser (MGL-W-532, Changchun New Industries Optoelectronics Technology Co., Ltd, China) operating at a wavelength of 532 nm was set up for high-speed shadow imaging. A high-speed camera (FASTCAM SA-Z, Japan) at a frame rate up to 200,000 fps @1024×1024 was used to photograph the sputtering of molten target. After passing through the sample, the 532 nm CW laser passed through three attenuators (each with 40% attenuation) and a narrow-band filter of 532 nm, and was finally amplified by a lens with a focal length of 100 mm for imaging into the high-speed camera. The analysis involves the sputtering of the molten target by the recoil pressure and/or shock wave, along with the laser supported combustion wave (LSCW).

Materials and characterization techniques

Alumina ceramic samples (96% Al_2O_3, Guangzhou Beilong Electronics Co., Ltd, China) have a thickness of 3 mm with a size of 30×30 mm^2. The original absorptivity of the alumina ceramic was tested to be 0.046 by using a Spectrophotometer (Hitachi model UH4150AD). In the damage of ceramic/metal composite material, 1 mm thick 304 stainless steel was placed at different locations (0 mm and 5 mm) below the 3 mm alumina ceramic (Fig. 1(b)). In addition, for sapphire damage, 1 mm thick sapphires (Guangzhou Beilong Electronics Co., Ltd, China) were used. The microstructures and chemical element distributions of the damaged target were characterized using a scanning electron microscope (SEM, MIRA4 LMH, TESCAN) equipped with an energy dispersive spectrometer (EDS, One Max 50). Each experiment was repeatedly 8 times.

Fluid dynamics simulations

The physical model describing the interaction between femtosecond-CW CPL and target was developed based on the theory of fluid dynamics and heat transfer, and analyzed by the COMSOL software with the modules "Heat transfer in fluid" and "Laminar two-phase flow, level set". To simulate the heat transfer and fluid dynamics of the CPL drilling, the Naiver-Stokes equations were solved through the finite element method and the Lever set method was used to track the moving interface. The air and alumina ceramic layer were assumed as incompressible Newtonian fluids flowing in a laminar way. In addition, the conservation of mass at the gas-liquid interface was broken when evaporation of the liquid alumina ceramic occurred during the drilling, so the mass conservation equation of the Naiver-Stokes equations was revised. Also, the control equations of the level set method were corrected. Additionally, a computational model of the pressure of the plasma shock wave induced by the femtosecond laser was constructed based on the Sedov-Taylor theory. This pressure model was integrated into the main body of the CW laser damage model of the target, serving as a volume force. This composite model facilitated the analysis of the change process of the melt pool under femtosecond-CW CPL damage and the impact of the femtosecond pulse shock wave pressure on the sputtering and temperature changes within the melt pool[41](a detailed description is provided in Appendix A, Supplementary information).

Results and discussion

Working principle and damage performance of the femtosecond-CW CPL

A filament structure (Fig. 2(a) and 2(b)), comprising a plasma column surrounded by an energy reservoir, is created under the competing processes of the Kerr self-focusing and the plasma defocusing[37]. A filament with a length of 30 mm is observed in the air by focusing the 1 mJ femtosecond laser using a mirror with a focal length of 500 mm, which can be divided into three parts, front, middle and tail. Along the propagation direction of the filament, it is observed that the diameter of the filament increases and then decreases, with the largest diameter near the middle (the diameter near the middle of the filament is ~30 μm). In addition, the tail of the filament is split into multiple small filaments from the original single filament (Fig. 2(c))[38].

No melting or vaporization of the original alumina ceramic occurs due to the low absorptivity of the original surface under the irradiation of the single CW laser with a power ranging from 400 to 900 W (Fig. S1). For the single femtosecond laser damage, a 4 mJ femtosecond laser irradiation for 1 s can only dorm a blind hole with a

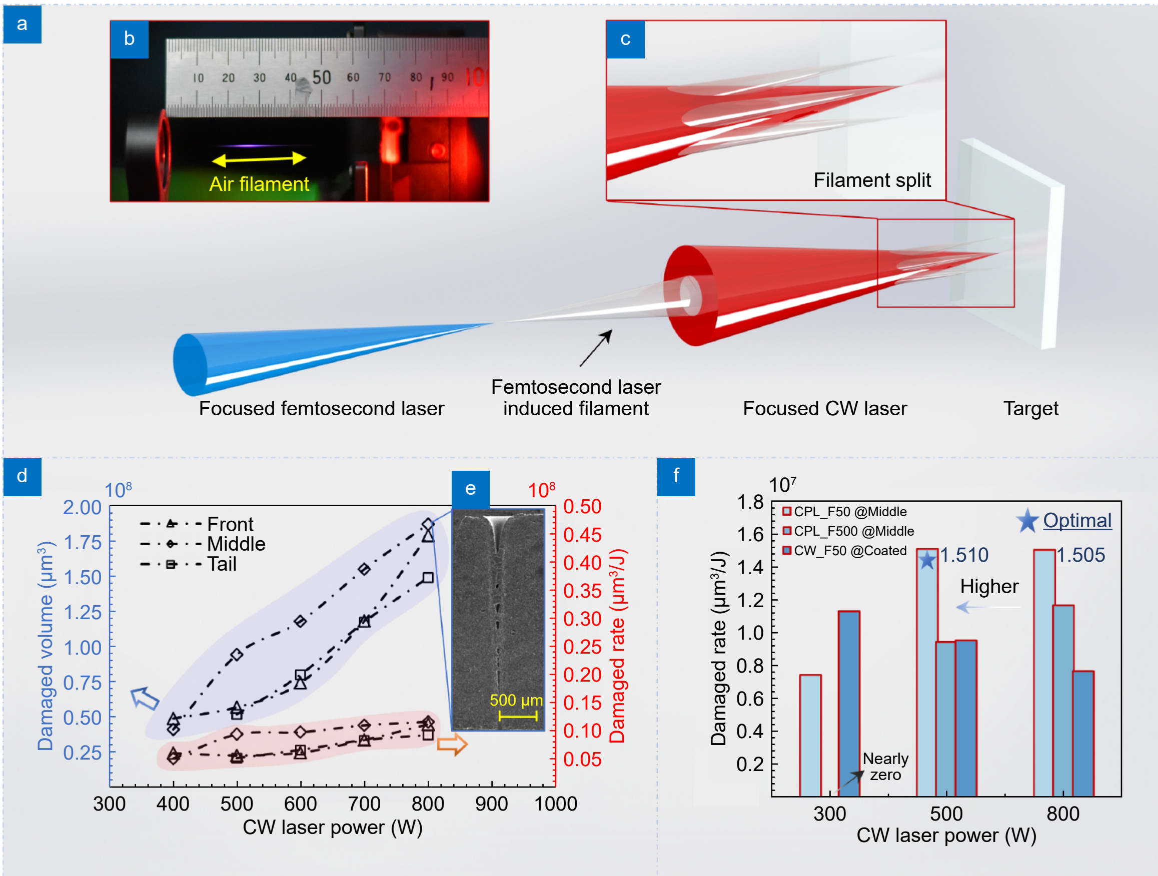

Fig. 2 | Femtosecond-CW CPL damage results. (**a**) Matching relationship of the spatial distribution of the two laser beams. The femtosecond laser with a single pulse of 1 mJ, and a damage time of 20 ms is adopt. (**b**) Spatial distribution morphology of the femtosecond laser-induced air filament. (**c**) Filament split phenomenon that appeared at the tail position of the filament. The diagram indicates that the position of the CW laser focus coincides with the tail position of the filament. (**d**) Damaged volume and rate that formed by CPL with different CW laser powers. The focal point of the CW laser is spatially coincident with the filaments at different positions (front, middle and tail). (**e**) Cross-section profile of the target that damaged by the femtosecond-CW CPL with an 800 W CW laser. A focusing lens with a focal length of 500 mm was used. (**f**) Comparison of the CPL damaged rate under different spatial-temporal parameter matching. F500 (F50) represents the use of a focusing lens with a focal length of 500 mm (50 mm). The CW_F50@coated represents the single CW laser damage rate obtained with the assistance of the carbon powder particle coating since the single CW laser was not able to ablate the original alumina ceramic surface (Fig. S1)[42].

diameter of 340 μm and a depth of 440 μm, and the optimal rate obtained by the femtosecond laser damage is 5.5×10^6 μm³/J[43,44]. The morphological differences produced when femtosecond laser induced filament irradiates on the target at different spatial positions are significant, with the highest ablation rate observed at the middle-filament (Fig. S2). In contrast to the damage achieved with the single CW laser or single femtosecond laser, the target is damaged through in 20 ms under the irradiation of femtosecond-CW CPL with a 400 W CW laser (Figs. 2 and S3). Notably, the front-filament damage exhibits the highest damage depth, whereas no significant damage performance is observed under the assistance of the tail-filament (Fig. S3(a)). The middle-filament damage achieves the largest damage diameter since the filament has the largest cross-sectional area while the peak power density is closer due to the power clamping. In addition, with a CW laser power exceeding 500 W, stable damage is attained with filament assistance in different positions, and all targets can be damaged through (Fig. S3(b)). Among them, the middle-filament assistance yields the maximum damaged volume when the CW power reaches 500 W or more, and the highest damage volume is obtained at 800 W CW laser (Fig. 2(d) and 2(e)). However, when the irradiated CW laser power is 300 W or lower, even with the assistance of middle-filament, no significant melting or vaporization occurs on the target surface. In this case, the ablation rate of the femtosecond-CW CPL is considered to be nearly zero (Fig. 2(f)).

For further improve the damage performance of the femtosecond-CW CPL, the CW laser focused spot size is further reduced to increase its laser fluence by using a focusing mirror with a focal length of 50 mm. The femtosecond-CW CPL can directly penetrate the whole target when the CW power is higher than 400 W (Fig. S4(a)). The damaged width in the hole upper and lower surface, and the damaged blind hole depth increases slowly with increasing CW laser power (Fig. S4(b)). The femtosecond laser-induced filament contributes to the sputtering of the target due to the excitation of a stronger plasma shock wave, depositing a larger diameter recast layer on the upper surface (Fig. S4(c) and S4(d))[44]. Also, sputtering traces appear at the contours of the melt deposited on the upper surface, further indicating that multiple sputtering behaviors occurred during the damage process with the recoil vapor pressure of the melt pool in conjunction with the femtosecond laser-induced shock wave[45]. In addition, the cross-section of the damaged hole is composed of the recast layer, the intermediate layer and the base material (Fig. S5(a–d)). Some small holes can be observed in the middle and lower part of the cross-section (Fig. S5(c)). The nanometer-sized particles are found in the middle of the hole, which is most likely due to the sputtering and deposition of particles formed by the local plasma breakdown of melt (Fig. S5(c)). The femtosecond laser can deposit on the air-melt interface while the melt moves below the hole with gravity to create a pore (Fig. S5(d)). Also, from the EDS results of the recast layer and the base material, the ratio of Al atoms to O atoms in the recast layer and the base material is also close to 2:3. It indicates that the ablation process is mainly a physical change of melting and vaporization of the material (Fig. S5(e) and S5(f)).

The damaged volume and rate are specifically compared for the three different CW laser powers (Fig. 2(f)). Experimental results indicate that the optimal damage performance is achieved under the middle-filament femtosecond-CW CPL mode (a focusing length of 50 mm, 1 mJ femtosecond laser, and 500 W CW laser), enabling complete penetration of a 3 mm thick target within 20 ms, with a damage rate of 1.51×10^7 μm³/J. In our experiments, if the single CW laser in the femtosecond-CW CPL is used for damage (100–900 W CW laser, Fig. S1), no significant surface damage is observed due to the low absorptivity of the target. Meanwhile, even with coating assistance, the damage rate of the CW laser reaches only 0.95×10^7 μm³/J when a same damage time of 20 ms is adopted[33,42].

Remarkably, these results highlight the significant advantages of the CPL damage method, as it not only overcomes the challenge of damaging alumina ceramics with the CW laser but also enhances the damage rate by 59% compared to coating-assisted CW laser (Fig. 2(f)) and by approximately 175% relative to a single femtosecond laser (5.5×10^6 μm³/J).

Transient dynamics of femtosecond-CW CPL-matter interaction

The uncoated target exhibits no discernible damage response under the irradiation of the single CW laser. In contrast, stable and efficient damage can be formed under the femtosecond-CW CPL, which represents that the CPL laser-target interaction process improves the absorption of the target material. In this regard, most of the existing studies suggest that the damage to the target under the CPL irradiation is formed transiently[19,29]. In this context, the dynamic damage process of the target under the irradiation of the femtosecond-CW CPL is observed and analyzed for the first time. Two CW average powers, 500 W and 800 W are used to combine with the 1 mJ femtosecond laser, and the damage processes monitored are shown as Fig. 3.

The effective damage of the target material is a gradual building process, i.e., the defect induction stage (Fig. 3(a) and 3(b)). There is an excited LSCW on the target surface observing the 1,000 μs moment under the irradiation of the femtosecond-CW CPL with an 800 W CW laser, and then this LSCW will gradually disappear (1,500 μs) with the turn-off of the femtosecond laser (Fig. 3(b)). The energy of the CW laser is effectively absorbed by the plasma that excited by the femtosecond laser at the initial damage stage, so that the LSCW can be excited at a suitable CW power (no LSCW is observed in the CPL damage with a 500 W CW laser, 1,000 μs). However, the plasma excited by the femtosecond laser is on the nanosecond time scale, so when the femtosecond laser is turned off, there is no long-lived plasma to maintain the absorption of the CW laser on the microsecond time scale.

Subsequently, the height of the LSCW can be observed to be gradually raised at the next femtosecond-CW CPL damage (2,000–5,000 μs). A defect induction stage, or called the keyhole formation phase, occurs

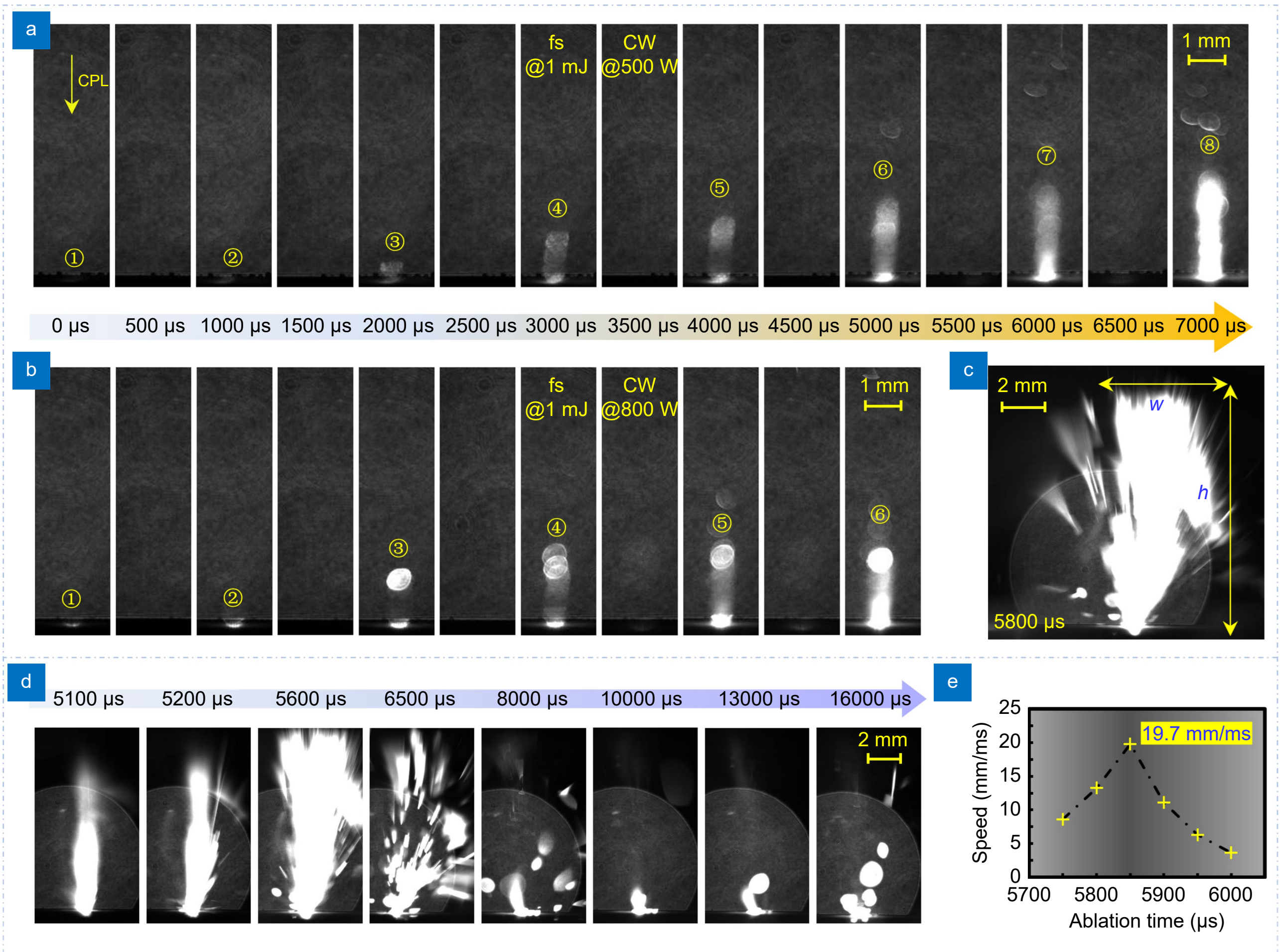

Fig. 3 | Femtosecond-CW CPL damage process monitoring by high-speed shadow imaging. Defect induction stage of the femtosecond-CW CPL damage process. The femtosecond-CW CPL combines the middle filament of the 1 mJ femtosecond laser and the (**a**) 500 W and (**b**) 800 W CW laser. (**c**) Sputtering of molten material formed on the target by femtosecond-CW CPL irradiation using an 800 W CW laser (5,800 μs). (**d**) Stable damage stage of the femtosecond-CW CPL damage process. (**e**) Analysis of the sputtering speed of the molten target during the femtosecond-CW CPL damage.

gradually during the CPL damage process. Specifically, at the irradiation of each CPL pulse, on the one hand, the femtosecond laser produces defects of different depths by direct damage of the target surface, and the multiple reflections of the defective hole wall can trigger a focusing effect to increase the laser fluence inside the hole[46]. Thus, with the continuous irradiation of the femtosecond-CW CPL, the defect depth gradually accumulates so that at a certain instant (i.e., 5,000 μs at 800 W CW laser), the focused CW laser fluence is sufficient to produce melting. Then, the sample surface starts to exhibit damage. An intense sputtering occurs under the dual action of the recoil pressure formed by the saturated vapor pressure and the femtosecond laser-induced shock wave (Fig. 3(c)). The LSCW achieved by the CPL with an 800 W CW laser has a width (w) of 5.0 mm and a height (h) of 11.6 mm.

The sputtering speed of the target is further analyzed during the intense damage sputtering stage (5,000–8,000 μs, Fig. 3(d)). The maximum sputtering speed is about 19.7 mm/ms (Fig. 3(e)). The plasma shock wave excited by the femtosecond laser mainly increases the sputtering volume, thus enhancing the damage performance. As well, when the target is melted through by the CPL, more laser energy will penetrate the sample directly, and the damage process enters a stable LSCW stage (8,000–16,000 μs, Fig. 3(d)). Only a small amount of molten material is sputtered from the upper surface. Overall, it is clear that CPL can efficiently prepare surface defects by 6 femtosecond-CW CPL pulses (5 ms) with an 800 W CW laser, which shows significant advantages in damage of ceramic-like transparent target.

The femtosecond-CW CPL damage of the alumina ceramic is analyzed by using the fluid dynamics model that considering the dynamic processes of the energy absorption, phase transformation, and micro-hole deformation process[47]. The assistance of shock wave created by the femtosecond laser-induced filament is added as a pressure of 28 MPa with a duration of 20 ns based on the Sedov-Taylor theoretical model[44]. The femtosecond-CW CPL consists of a 300 W CW laser with a 1 mJ femtosecond laser is adopted because the target is not penetrated through, which avoids the errors caused by the direct loss of laser energy and the quantitative measurement of the penetration time (Fig. S4(a)). The damage process of the femtosecond-CW CPL with a 300 W CW laser is analyzed by high-speed shadow imaging, and it is found that 10 CPL pulses are required to create the defect and then starts the hole damage. In the case of setting the damage time to 20 ms in the experiment, the actual effective damage time is about 11 ms, containing 10 shock waves added to the model at 1 ms, 2 ms, ..., and 10 ms, respectively. The surface absorptivity can be set to 1.0 since the defect will saturate the laser absorption[47].

The temperature change of the melt pool during the whole damage process is shown in Fig. 4(a) and 4(b). The melt pool reaches the melting temperature at ~500 μs and the vaporization temperature at ~750 μs. Subsequently, it can be observed that the temperature does not keep a constant rise but oscillates around the vaporization temperature. Sputtering of the melt pool occurs when the femtosecond laser-induced shock wave acts on the melt pool. There is a brief drop in the temperature of the melt pool since the melt sputtering process take away the high temperature molten material[23]. At the same time, the more violent the sputtering, the more heat is taken away, and the more the temperature of the melt pool drops. The melt pool temperature drops by about 509 K under the sputtering of the first shock wave, 460 K under the second shock wave, and the sputtering effect brought by the shock wave can be considered to be gradually weakening (Fig. 4(c)). The melt pool temperature only decreased by 20 K when the fifth shock wave is applied (Fig. 4(d)). Thereafter, the contribution of the shock wave to the enhanced sputtering effect of the melt pool is almost negligible, and the subsequent five shock waves in Fig. 4(a) do not cause a significant temperature drop in the melt pool. The phenomenon is consistent with the sputtering effect observed by high-speed shadow imaging.

In addition, after 50 μs (loading the shock wave at 1 ms), the melt pool depth increases from 35 μm to 132 μm and the width increases from 170 μm to 350 μm (Fig. 4(b)),

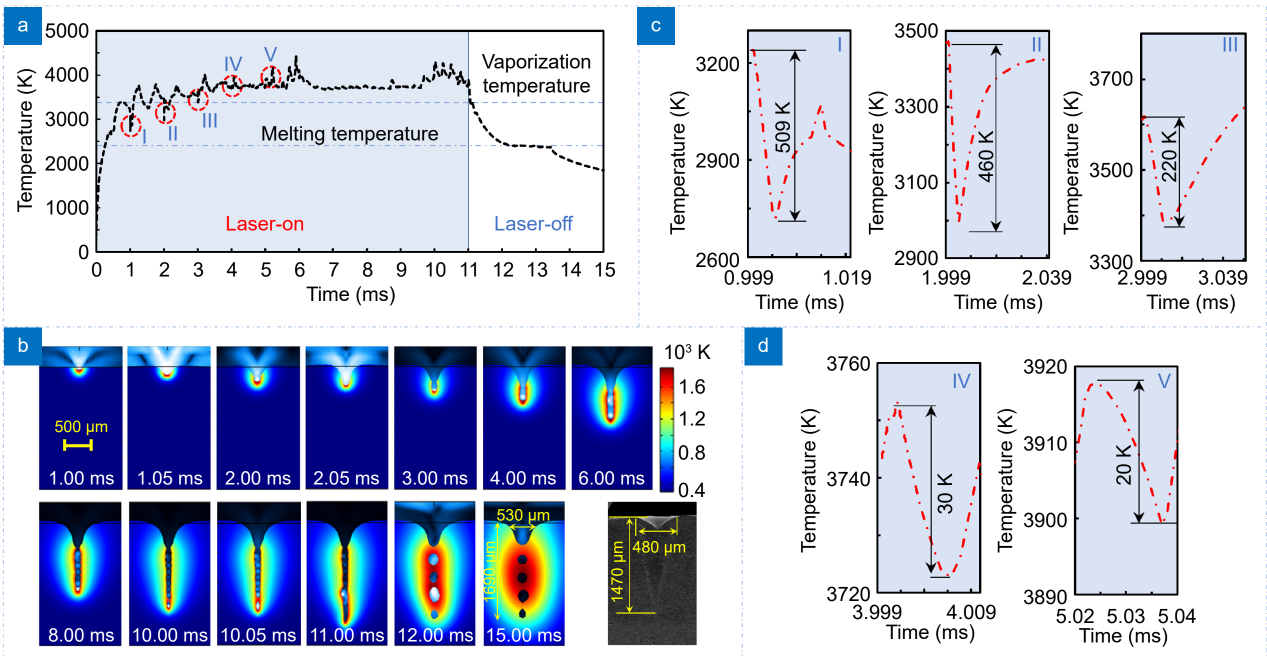

Fig. 4 | Numerical analysis of the femtosecond-CW CPL damage of alumina ceramic. (**a**) Temperature change of the target under the irradiation of the femtosecond-CW CPL. (**b**) Evolution of melt pool morphology of target under the irradiation of the femtosecond-CW CPL. (**c**, **d**) Transient changes in the melt pool temperature under the sputtering of the first 5 femtosecond laser-induced shock waves.

which indicates that the shock wave shows a good effect on the melt pool sputtering in the initial damage stage. However, with the increase of the melt depth, the molten material escapes from the damage hole by a longer stroke, which requires more sputtering energy to achieve the exclusion. Also, the increase of the melt pool depth will form an elastomer inside, and the loss of stable fulcrum for sputtering will also lead to a poor sputtering effect. Therefore, as the damage time increases, the sputtering effect of the shock wave on the melt pool will also be weakened. As observed in the shadow imaging, the sputtering of the melt pool by the later femtosecond pulses is not significant. At the time of 12.0 ms when the laser is turned off, the molten material flows back into the hole and leads to blocking, which is also close to the cross-section profile in the experimental results (Fig. S4(a)).

Multi-applications of femtosecond-CW CPL damage method

Moreover, alumina ceramic exhibits transparent properties to the laser irradiation after it is penetrated through, and the ability of the penetrating laser irradiation to further damage the subsequent target deserves further investigation, e.g. direct damage to the circuitry behind ceramic structural body. A metal target (using 304 stainless steel targets as an example) is selected and placed at distance of D mm from the back of the alumina ceramic (Fig. 5(a)). The CW laser power is set to 500 W, the single pulse energy of the femtosecond laser is set to 1 mJ and 2 mJ.

The metal target damage results obtained for different sample distance (0 mm, 5 mm) and different damage times (15 ms, 20 ms, and 25 ms) are shown in Fig. 5(b).

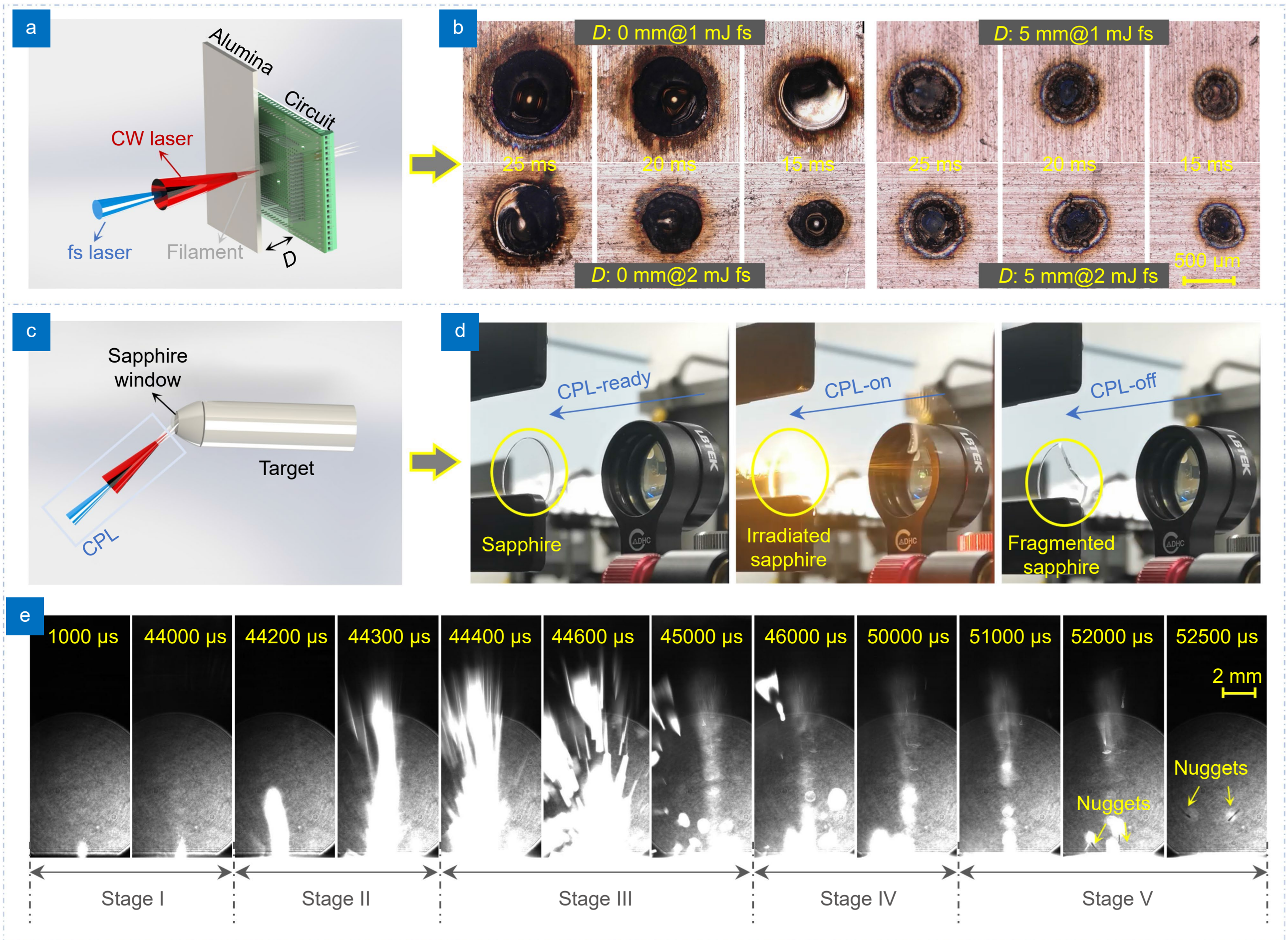

Fig. 5 | Application of the femtosecond-CW CPL damage method. (**a**) Schematic of the CPL penetration damage to the ceramic/metal composite material, where CPL penetrates the structural ceramic and then damages the circuit structure behind it. (**b**) Melt penetration damage properties of femtosecond-CW CPL. A metal target is placed behind the alumina ceramic with a distance (0 and 5 mm). (**c**) Schematic of CPL damage to a sapphire window mirror. (**d**) The process of femtosecond-CW CPL damage to the sapphire using an 800 W CW laser. (**e**) Damage process monitored by the high-speed shadow imaging. Stage I, defined as the defect induction stage. Stage II, damage build-up stage. Stage III, intense sputtering stage. Stage IV, the impact stage of the femtosecond laser-induced shock wave. Stage V, target blow-up stage.

The damage traces can all be observed on the metal surface, further demonstrating the transparent properties of molten alumina ceramics to the laser. Sputtering traces from the femtosecond laser can also be observed (Fig. 5(b)). As mentioned earlier, the CPL uses 7 ms for defect formation when using 500 W CW laser, so when the selected time is 15 ms for penetration damage, the damage time with the metal target is less than 8 ms. As shown in the Fig. 5(b), a melt diameter of 200 μm can be observed even at a 5 mm distance, and a molten area of 700 μm in diameter can be observed when the selected distance is 0 mm and damage time is 25 ms. In addition, when comparing the femtosecond-CW CPL damage results using 1 mJ and 2 mJ femtosecond lasers for penetrating damage, it can be noted that the melt diameter of the metal surfaces reduced with the assistance of the 2 mJ femtosecond laser. The stronger the plasma generated on the alumina ceramic under the irradiation of the 2 mJ femtosecond laser, the more significant the shielding effect on the CW laser, thus leading to an overall reduction in the melt diameter of the metal target. Also, the proposed femtosecond-CW CPL method is also applied to damage real ceramic/circuit target, demonstrating excellent damage performance (Fig. S6).

Finally, we further demonstrate the efficient damage performance of the CPL on transparent target (sapphire window mirror, Fig. 5(c)). One of the characteristics of sapphire is that it has good transmittance for multi-band light and is one of the material choices for multiple types of window mirrors[48]. Existing damage methods such as high-energy CW laser are almost difficult to form an effective damage due to the extremely low absorption of the sapphire target. For the CPL damage to the sapphire with a thickness of 1 mm, the CW laser power is set to 800 W, and the single pulse energy of the femtosecond laser is set to 1 mJ. A blind hole with a depth of 160 μm and a diameter of 121 μm is obtained by using the 1 mJ femtosecond laser (Fig. S7(a)), and the direct fragmentation of sapphire is achieved by using the CPL with a damage time of 100 ms (Fig. S7(b)).

The absorptivity of CW laser in the infrared band is less than 1%, so the CW laser energy cannot be absorbed by the sapphire directly. However, after the femtosecond laser creates defects on the sapphire surface under the irradiation of the femtosecond-CW CPL, the absorptivity of the CW laser by the defect increases dramatically. Figure 5(d) depict the ablation processes of sapphire using femtosecond-CW CPL with an ablation time of 100 ms. Figure 5(e) illustrates the CPL-sapphire interaction at different ablation process using the high-speed shadow imaging, and the femtosecond-CW CPL is capable of causing the direct fragmentation of the sapphire target within 52,500 μs, which can be divided into five stages.

The first defect induction stage, in which the femtosecond laser creates the defect to improve the absorption. It lasts approximately 44 ms, with a total of 45 femtosecond-CW CPL pulses irradiating on the sapphire surface. The second stage is the ablation build-up process stage. After 45 CPL pulses creating defects, the sapphire absorbs the CW laser with a higher pulse energy. The heat accumulation on the sapphire surface makes the temperature reaches the ablation threshold, which lasts for about 300 μs. From 44,400 μs onward, violent sputtering stage occurs under the impact of the shock wave induced by the femtosecond laser, with material also sputtered from the lower surface, indicating penetration of the sample (Fig. S8). After the violent sputtering stage, the sputtering on the front side of the sample has almost stopped and the sputtering on the back side of the sample is increasing. The thermal stress around the ablation hole is accumulating under the impact of the femtosecond laser-induced shock wave for a total duration of about 5,000 μs. Finally, the femtosecond-CW CPL ablation process enters the fifth stage (direct fragmentation). After the accumulation of thermal stress in the fourth stage and the combined effect of the pressure induced by the plasma shock wave, the final thermal stress is greater than the material binding strength of the sapphire target, causing the direct fragmentation of the sample (nuggets marked in the Fig. 5(e))[49].

Discussions on the prospective applications of the femtosecond-CW CPL damage method

This work leverages the long-range and high-peak transmission capabilities of femtosecond laser-induced air filament to address the practical challenges of CP damage method. Under our experimental conditions, a focusing length of up to 500 mm is tested. Although this condition does not yield the optimal MRR, it still reaches 1.2×10^7 μm^3/J (Fig. 2(f), 800 W), significantly surpassing the damage performance of both single-beam CW and femtosecond laser. Thus, within the current experimental framework, we have demonstrated the potential of femtosecond laser induced air filament-CW CPL for long-range damage applications, particularly in the destruction of highly damage-resistant transparent materials. In the future, employing femtosecond laser with higher repetition rates and pulse energies to generate more sustained and longer-propagating filament, and considering injecting collimated CW laser into the filament will unlock vast new possibilities for this approach (Fig. S9).

In terms of specific damage performance metrics, this study demonstrates that CPL can achieve efficient damage of alumina ceramics, penetration damage of ceramic/metal composite material, and the direct fragmentation of sapphire target, all of which are novel findings. It is well known that the power clamping effect is a core issue limiting the damage efficient of femtosecond laser induced air filament, and thus these phenomena can be re-examined from the perspective of femtosecond laser induced air filament. Firstly, in the efficient damage of alumina ceramic with the assistance of CW laser, our findings show that CPL achieves a maximum MRR of 1.5×10^{7} μm^3/J. If we focus only on the femtosecond laser energy used, the damage rate of the femtosecond-CW CPL is improved by about 3 orders of magnitude compared to the single femtosecond laser. Therefore, CPL effectively overcomes the efficiency limitation caused by the power clamping effect of the filament. Secondly, in the damage of alumina ceramic-metal composite materials, CPL can penetrate 3 mm of alumina ceramic and achieve efficient damage to the underlying metal, while a single femtosecond laser, even with an irradiation time of up to 1 s, can only form small holes a few hundred micrometers deep. This demonstrates that CPL effectively overcomes the limitation on energy transfer caused by the plasma shielding induced by the filament. Finally, CPL has achieved direct fragmentation of sapphire target. To the best of our knowledge, this is the first report of such an effect, greatly demonstrating the potential of CPL in the transient damage of transparent materials.

For structural and functional ceramic materials, we systematically revealed the damage mechanisms of the proposed CPL method for various target types. Based on high-speed imaging and multiphase flow simulation models, we first confirmed that the CPL pulses contribute to the gradual formation of defect that improves the absorptivity of the CW laser, so the femtosecond-CW CPL is able to damage the target with a lower CW laser fluence. We also observed that the coaxially transmitted CW laser has little effect on the femtosecond laser-induced filament state. However, the plasma formed by the filament on the target surface clearly shields the absorption of the CW laser, thus affecting its energy deposition to the target. Additionally, the spatial position of the filament significantly affects the performance when assisting CW laser in target damage. The middle of the filament achieves the largest ablation volume, while the front filament, due to weaker plasma shielding, can more efficiently utilize energy and has advantages in forming deeper damage. The tail filament, however, suffers from multi-filament splitting and plasma shielding issues, showing the poorest performance in assisting the CW laser.

Finally, we also consider whether the proposed femtosecond laser induced air filament-CW CPL method could have significant advantages in laser processing. Although the damage morphology in our work—such as hole taper, recast layer, and surface quality—may not be ideal from a micro-nano processing perspective, it is clear that our approach, due to the unique properties of femtosecond filament, presents notable advantages for long-distance and deep-depth processing applications. For instance, we test alumina ceramics with thicknesses ranging from 5 mm to 8 mm, and the CPL is able to transiently form through-holes in all cases. We believe that for laser processing of samples with large thicknesses, such as drilling and cutting, this CPL method will lead to new technological breakthroughs, with potential applications in areas like long-distance steel plate cutting for rescue operations in public safety.

Conclusions

In response to the difficulty of existing high-energy CW laser damage of structural or functional ceramics, we have achieved efficient and stable CW laser damage of ceramic materials for the first time with the assistance of a femtosecond laser-induced air filament. Using the proposed femtosecond-CW CPL damage method (combining 1 mJ femtosecond laser and 500 W CW laser), a 3 mm thickness target can be damaged through in a time of 20 ms with a damage rate of 1.51×10^{7} μm^3/J, which is 59% higher than with the coating-assisted CW laser damage and 175% higher than with the single femtosecond laser damage. In order to investigate the intrinsic mechanism of femtosecond-CW CPL damage of the ceramics, high-speed shadow imaging and multiphase flow simulation models are elaborated and analyzed. The simulation results are in high agreement with the experimental results, confirming that the sputtering effect of the femtosecond laser filament induced shock wave is the main mode of material removal in CPL damage. Finally, melt penetration damage and sapphire damage by the proposed femtosecond-CW CPL method are also revealed, and it is confirmed that the femtosecond-CW CPL method has great advantages in the damage a wide range of targets.

Considering that femtosecond-CW CPL can improve the laser absorption of the target material, while also allows efficient sputtering of molten material by inducing shock waves, and combined with the spatial filamentation and transmission characteristics of the femtosecond laser, it is promising to be the next generation of new methods for target damage, especially for transparent hard and brittle materials.

References

1. Lin ZY, Hong MH. Femtosecond laser precision engineering: from micron, submicron, to nanoscale. *Ultrafast Sci* **2021**, 9783514 (2021).
2. Penilla EH, Devia-Cruz LF, Wieg AT et al. Ultrafast laser welding of ceramics. *Science* **365**, 803–808 (2019).
3. Li LJ, Gattass RR, Gershgoren E et al. Achieving λ/20 resolution by one-color initiation and deactivation of polymerization. *Science* **324**, 910–913 (2009).
4. Gu DD, Shi XY, Poprawe R et al. Material-structure-performance integrated laser-metal additive manufacturing. *Science* **372**, eabg1487 (2021).
5. Jin J, Geng SN, Shu LS et al. High-strength and crack-free welding of 2024 aluminium alloy via Zr-core-Al-shell wire. *Nat Commun* **15**, 1748 (2024).
6. Zuo JX, Lin XC. High-power laser systems. *Laser Photonics Rev* **16**, 2100741 (2022).
7. Jia XS, Luo JL, Li K et al. Ultrafast laser welding of transparent materials: from principles to applications. *Int J Extrem Manuf* **7**, 032001 (2025).
8. Li J, Zhong S, Huang JX et al. Laser-guided anisotropic etching for precision machining of micro-engineered glass components. *Int J Mach Tools Manuf* **198**, 104152 (2024).
9. Wang JS, Fang FZ, An HJ et al. Laser machining fundamentals: micro, nano, atomic and close-to-atomic scales. *Int J Extrem Manuf* **5**, 012005 (2023).
10. Sun K, Tan DZ, Fang XY et al. Three-dimensional direct lithography of stable perovskite nanocrystals in glass. *Science* **375**, 307–310 (2022).
11. Tang HC, Men T, Liu XL et al. Single-shot compressed optical field topography. *Light Sci Appl* **11**, 244 (2022).
12. Lian YL, Jiang L, Sun JY et al. Ultrafast quasi-three-dimensional imaging. *Int J Extrem Manuf* **5**, 045601 (2023).
13. Obata K, Caballero-Lucas F, Kawabata S et al. GHz bursts in MHz burst (BiBurst) enabling high-speed femtosecond laser ablation of silicon due to prevention of air ionization. *Int J Extrem Manuf* **5**, 025002 (2023).
14. Li ZZ, Fan H, Wang L et al. Super-stealth dicing of transparent solids with nanometric precision. *Nat Photonics* **18**, 799–808 (2024).
15. Li XB, Ye BC, Jiang L et al. Helical micropillar processed by one-step 3D printing for solar thermal conversion. *Small* **20**, 2400569 (2024).
16. Zhu DZ, Xie JW, Yan JF et al. Ultrafast laser plasmonic fabrication of nanocrystals by molecule modulation for photoresponse multifunctional structures. *Adv Mater* **35**, 2211983 (2023).
17. Zhao M, Wen J, Hu Q et al. A 3D nanoscale optical disk memory with petabit capacity. *Nature* **626**, 772–778 (2024).
18. Liu HG, Lin WX, Hong MH. Hybrid laser precision engineering of transparent hard materials: challenges, solutions and applications. *Light Sci Appl* **10**, 162 (2021).
19. Jia XS, Chen YQ, Liu L et al. Combined pulse laser: Reliable tool for high-quality, high-efficiency material processing. *Opt Laser Technol* **153**, 108209 (2022).
20. Fox JA. A method for improving continuous wave laser penetration of metal targets. *Appl Phys Lett* **26**, 682–684 (1975).
21. Jia XS, Zhu GZ, Zhang YD et al. Laser processing of alumina ceramic by spatially and temporally superposing the millisecond pulse and nanosecond pulse train. *Opt Express* **28**, 676–684 (2020).
22. Yoshitake S, Ito Y, Miyamoto N et al. Ultrafast and large-gap microwelding of glass substrates by selective absorption of continuous-wave laser into transiently excited electrons. *CIRP Ann* **71**, 157–160 (2022).
23. Qin Y, Förster DJ, Weber R et al. Numerical study of the dynamics of the hole formation during drilling with combined ms and ns laser pulses. *Opt Laser Technol* **112**, 8–19 (2019).
24. Pan YX, Lv XM, Zhang HC et al. Millisecond laser machining of transparent materials assisted by a nanosecond laser with different delays. *Opt Lett* **41**, 2807–2810 (2016).
25. Lv XM, Pan YX, Jia ZC et al. Laser-induced damage threshold of silicon under combined millisecond and nanosecond laser irradiation. *J Appl Phys* **121**, 113102 (2017).
26. Liu XQ, Bai BF, Chen QD et al. Etching-assisted femtosecond laser modification of hard materials. *Opto-Electron Adv* **2**, 190021 (2019).
27. Pan YX, Zhang HC, Chen J et al. Millisecond laser machining of transparent materials assisted by nanosecond laser. *Opt Express* **23**, 765–775 (2015).
28. Ito Y, Yoshizaki R, Miyamoto N et al. Ultrafast and precision drilling of glass by selective absorption of fiber-laser pulse into femtosecond-laser-induced filament. *Appl Phys Lett* **113**, 061101 (2018).
29. Miyamoto N, Ito Y, Wei CR et al. Ultrafast internal modification of glass by selective absorption of a continuous-wave laser into excited electrons. *Opt Lett* **45**, 3171–3174 (2020).
30. Temmler A, Liu DM, Drinck S et al. Experimental investigation on a new hybrid laser process for surface structuring by vapor pressure on Ti6Al4V. *J Mater Process Technol* **277**, 116450 (2020).
31. Wei CR, Yoshizaki R, Ito Y et al. High-speed microgroove processing of glass by expanding the high-temperature region formed by transient and selective laser absorption. *Opt Express* **30**, 32280–32291 (2022).
32. Zhou R, Lin SD, Ding Y et al. Enhancement of laser ablation via interacting spatial double-pulse effect. *Opto-Electron Adv* **1**, 180014 (2018).
33. Jia XS, Lin JW, Li Z et al. Continuous wave laser ablation of alumina ceramics under long focusing condition. *J Manuf Processes* **134**, 530–546 (2025).
34. Jia XS, Dong J, Chen YQ et al. Laser processing of alumina

ceramic by a spatially superposing millisecond laser and a nanosecond laser with different beam shapes. *Appl Opt* **59**, 7195–7200 (2020).
35. Kerrigan H, Masnavi M, Bernath R et al. Laser-plasma coupling for enhanced ablation of GaAs with combined femtosecond and nanosecond pulses. *Opt Express* **29**, 18481–18494 (2021).
36. Kasparian J, Rodriguez M, Méjean G et al. White-light filaments for atmospheric analysis. *Science* **301**, 61–64 (2003).
37. Durand M, Houard A, Prade B et al. Kilometer range filamentation. *Opt Express* **21**, 26836–26845 (2013).
38. Valenzuela A, Munson C, Porwitzky A et al. Comparison between geometrically focused pulses versus filaments in femtosecond laser ablation of steel and titanium alloys. *Appl Phys B* **116**, 485–491 (2014).
39. Wang FF, Pan CJ, Sun JY et al. Direct observation of structure-assisted filament splitting during ultrafast multiple-pulse laser ablation. *Opt Express* **27**, 10050–10057 (2019).
40. Juodkazis S, Nishimura K, Misawa H et al. Control over the crystalline state of sapphire. *Adv Mater* **18**, 1361–1364 (2006).
41. Li Z, Yang Z, Jia XS et al. Numerical analysis of the effect of temporal and/or spatial shaping on the ms/ns combined pulse laser drilling performance of alumina ceramic. *Opt Laser Technol* **164**, 109481 (2023).
42. Jia XS, Luo JL, Guo C et al. High-energy continuous wave laser ablation of alumina ceramic. *J Mater Res Technol* **27**, 5389–5403 (2023).
43. Li Z, Lin JW, Wang CGN et al. Damage performance of alumina ceramic by femtosecond laser induced air filamentation. *Opt Laser Technol* **181**, 111781 (2025).
44. Li Z, Lin JW, Jia XS et al. High efficiency femtosecond laser ablation of alumina ceramics under the filament induced plasma shock wave. *Ceram Int* **50**, 47472–47484 (2024).
45. Jia XS, Zhu GZ, Wang HL et al. Characterization of micro-holes drilled in alumina ceramic by the combined pulse laser technique. *Appl Opt* **59**, 6161–6167 (2020).
46. Jia XS, Chen YQ, Wang HL et al. Experimental study on nanosecond-millisecond combined pulse laser drilling of alumina ceramic with different spot sizes. *Opt Laser Technol* **130**, 106351 (2020).
47. Jia XS, Li Z, Wang C et al. Study of the dynamics of material removal processes in combined pulse laser drilling of alumina ceramic. *Opt Laser Technol* **160**, 109053 (2023).
48. Ding YL, Liu LP, Wang C et al. Bioinspired near-full transmittance MgF_2 window for infrared detection in extremely complex environments. *ACS Appl Mater Interfaces* **15**, 30985–30997 (2023).
49. Lv XM, Pan YX, Jia ZC et al. Surface damage induced by a combined millisecond and nanosecond laser. *Appl Opt* **56**, 5060–5067 (2017).

Acknowledgements

We are grateful for financial supports from National Natural Science Foundation of China (Grant No. 52105498), The science and technology innovation Program of Hunan Province (Grant No. 2021RC3074). Advanced Laser Technology Laboratory of Anhui Province (AHL2022KF04), National Key R&D Program of China (Grant No. 2023YFB14605500), and Changsha Natural Science Foundation (kq2402089).

Author contributions

K. H., J. D., and X. J. conceived the idea and supervised the project; C. G., K. L., Z. Liu, Y. C., J. X. and Z. Li. constructed the system and performed the experiment; W. C., C. S., and C. W. helped perform the analysis; Z. Li. and X. J. helped performed the experiment and data analyses.

Competing interests

The authors declare no competing financial interests.

Supplementary information

Supplementary information for this paper is available at
https://doi.org/10.29026/oea.2025.240296

Scan for Article PDF